Multimodal spectroscopic investigation of the conformation and local environment of biomolecules at an electrified interface

Sasha A Moonitz[1], Noah Shepard[1], Rodrigo Noriega[1,*]

[1] University of Utah, Department of Chemistry, 315 S. 1400 E. Salt Lake City, UT 84112

* Email: noriega@chem.utah.edu

Abstract

The complex and dynamic interfacial regions between biological samples and electronic components pose many challenges for characterization, including their evolution over multiple temporal and spatial scales. Spectroscopic probes of buried interfaces employing mid-infrared plasmon resonances and time-resolved fluorescence detection in the visible range are used to study the properties of polypeptides adsorbed at the surface of a working electrode. Information from these complementary spectroscopic probes reveals the interplay of solvation, electric fields, and ion concentration on their resulting macromolecular conformations.

Introduction

Interfaces are ubiquitous in biological systems and in biomedical devices,[1–4] and such interfacial regions are dynamic environments which evolve over multiple time scales – from sub-picosecond molecular motions to microsecond cellular events and even slower biological and chemical processes.[4–8] Moreover, phase boundaries are often electrically charged and experience strong concentration gradients of ionic solutes.[5] It is within this complex environment that processes involving the assembly of biomolecules at phase boundaries take place – e.g., the formation of bioelectronic interfaces and the growth of biofilms.[3,7,9–11] Because interfaces are critical components in sensors and stimuli delivery devices, it is relevant to develop novel experimental platforms to probe the interactions between conformationally flexible biomolecules, their dynamic solvent environment, and ionic species under the effect of electric fields.

The characterization of interfaces is a challenging feat due in part to their small spatial extent compared to bulk material, the large heterogeneity in their composition and morphology, and their continuous evolution over time. In particular, buried interfaces are difficult to characterize nondestructively and under operating conditions. To date, a variety of tools – from scanning probe microscopy to visible and infrared linear and nonlinear spectroscopies – have been developed to interrogate biological interfaces and measure properties such as their chemical structure,[12,13] morphology,[14–17] and formation kinetics.[17–20] In recent years, it has become clear that advancing our understanding of complex mixtures at heterogeneous interfaces and in the presence of external stimuli requires the combination of multiple experimental techniques that provide complementary information with interfacial sensitivity.[20–23] Importantly, in order to study hierarchical

transformations that link molecular-scale events to phenomena at the mesoscopic and macroscopic scales, characterization tools should be able to probe fast processes (10^{-12}-10^{-6} s). Beyond these temporal resolution and surface-sensitivity requirements, in order to enable the broadest possible applicability it is desirable to pursue experimental platforms that do not impose stringent constraints on materials properties (e.g., nonlinear polarizabilities, HOMO/LUMO level alignment) or on sample geometry (e.g., high surface area, specific crystalline facets).

To this effect, we have developed an experimental platform that combines time-resolved fluorescence spectroscopy with mid-infrared surface plasmon resonances launched by ultrafast laser pulses at an active electrochemical interface. This combination of characterization techniques is made possible by wide band gap degenerate metal oxide semiconductor films (indium tin oxide, ITO), which can simultaneously act as a plasmonic medium with strong resonances in the mid-infrared,[24–32] as the working electrode in an electrochemical cell or biosensor,[33,34] and as a transparent window in the UV-vis-NIR range for optical excitation and fluorescence collection.[35] We employ the capabilities of these two complementary interface-sensitive spectroscopic tools to detect the electric-field assisted adsorption of polypeptide layers at a solid/liquid interface, the changes in their hydration state, and the electric field perturbation of their molecular conformations and solvation environment. The signatures of coupled processes involving the intercalation of solvent molecules and ions in the adsorbed layer and the collective changes in conformation of polypeptide chains are detected by correlating surface plasmon reflectivity with time-resolved fluorescence brightness, lifetime, and anisotropy.

We find that the properties of adsorbed polypeptides are not only dependent on bulk solvent properties, but they can be modulated with interfacial electric fields.

Experimental

Materials and Methods

Materials. Details on the deposition of ITO films, preparation of buffered solutions and samples can be found in the Supporting Information.

Optical and electrical properties of ITO films. After ITO deposition, a subset of sacrificial substrates were characterized with a combination of structural, optical, and electrical measurements. ITO film thicknesses between 120-200 nm were measured with a stylus profilometer (Tencor P-10), and their root-mean-square surface roughness was found to be ≤ 2.15 nm using atomic force microscopy (Bruker Dimension Icon, **Fig. S1**). Spectroscopic ellipsometry was employed to extract complex refractive indices for the film stack (**Fig. S2**). A Drude model was used to describe the ITO optical properties, with typical values for plasma frequency and damping coefficient of $\omega_p = 2.2 - 3.1 \times 10^{15}$ Hz and $\Gamma \sim 2.5 \times 10^{14}$ Hz, respectively (free carrier density $n_e = 0.5 - 1.1 \times 10^{21}$ cm^{-3}). Conductivity measurements with a 4-point probe (Microtech RF-1) yield sheet resistances of 10-30 Ω/□, in agreement with thickness and doping values obtained with optical characterization. Substrates had a high transmittance (~85%) in the visible spectral range.

Mid-IR plasmonic response of ITO SPR chips. Reflectivity curves were acquired for ITO SPR chips in contact with simple dielectric media (air, water, methanol). All SPR

measurements were taken in the Kretschmann configuration (**Fig. 1**) – experimental and modeling details are provided in the Supporting Information. The plasmonic behavior of ITO substrates can be described with a simple dielectric stack model yielding similar parameters as those obtained from spectroscopic ellipsometry. Importantly, sharp plasmonic resonances are observed using ultrafast pulsed sources in the mid-IR. Sensitivity estimates (**Fig. S3**) agree with model predictions and enable detection of small changes in interfacial properties, as discussed below.

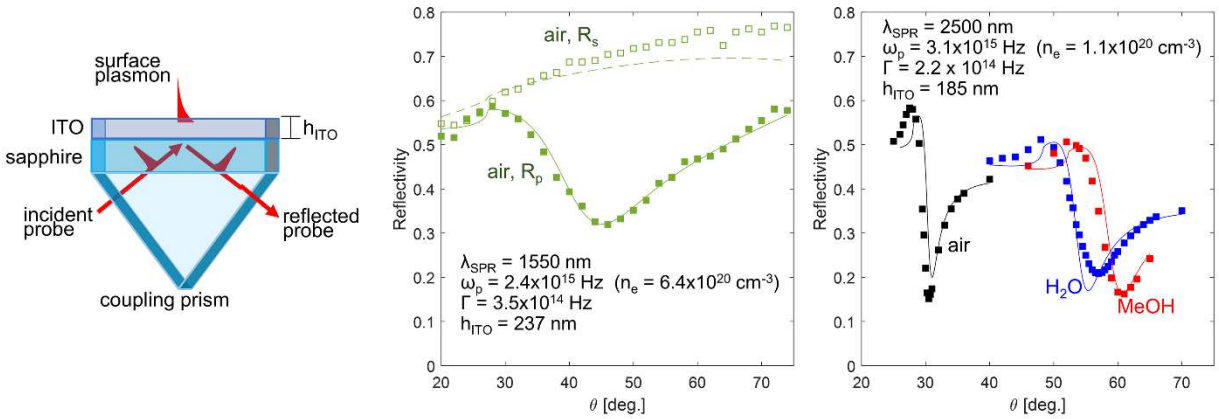

Figure 1. **Surface plasmon resonances in the mid-IR can be supported by degenerately doped ITO films, even when in contact with condensed phases.** The reflectivity of a probe as a function of incident angle is measured in the Kretschmann configuration (left panel). The plasmonic nature of these resonances is evidenced by the characteristic reflectance minimum for incident beams with *p*-polarization but no resonance for *s*-polarized light (center panel). These SPR resonances are much sharper at longer wavelengths, and optimization of experimental geometry and materials parameters enable probing of condensed phases (right panel). Drude metal model parameters for ITO are shown in the center and right panels (ITO films deposited under different conditions). Markers are data, and lines are modeled SPR curves.

SPR measurements of polypeptide adsorption. Before electric-field assisted polypeptide adsorption, a full trace of reflectivity vs. incidence angle is taken in air followed by two curves in solvents of different refractive index (buffer solution and methanol). These

94 preliminary data serve as a benchmark for the response of each individual ITO mid-IR
95 SPR chip. Using these results, a sensing angle is selected for further data collection (to
96 minimize errors due to detector re-positioning). Changes in reflectivity at constant sensing
97 angle are then measured as a function of voltage and buffer conditions. Surface potentials
98 at the ITO working electrode are applied with a CH Instruments bipotentiostat using a Pt
99 counter electrode and a Ag/AgCl quasi-reference electrode (**Fig. S4**).

100 *Time-resolved fluorescence of adsorbed polypeptide layers.* Low-background
101 fluorescence measurements of chromophore-labeled polypeptides adsorbed on ITO were
102 performed using a polarization-resolved ultrafast fluorescence instrument with few
103 modifications from a previously described setup.[36] The electrostatic potential at the ITO
104 surface is controlled with the same electrochemical setup used for SPR measurements.
105 Instrumental and data analysis details are provided in the Supporting Information and
106 **Fig. S5**.

107

108 **Results and discussion**

109 *Field-enhanced adsorption and environment-dependent hydration of adsorbed*
110 *polypeptides at an electrode.* The interfacial adsorption of charged polypeptides under
111 the effect of electric fields has been previously reported using optical waveguide loss
112 spectroscopy and correlated to quartz crystal microbalance experiments.[19,37,38] Here, we
113 exploit the adhesion of poly-L-lysine (PLL) onto an electrified surface to characterize its
114 conformational transformations upon pH changes and as a function of an interfacial
115 electric field. We observe irreversible adsorption of PLL from a high ionic strength

116 (I=1.2 M) pH=11 Britton-Robinson buffer at positive potentials (**Fig. 2**). After adsorption is
117 saturated at large positive surface potentials, no change in reflectivity was observed upon
118 further changes in voltage. These PLL adsorbates cover ~3-10% of the ITO substrate and
119 have a layer height of ~80 nm (**Fig. S6**). Dielectric stack modeling of the SPR response
120 allows the extraction of dielectric constant for the PLL adsorbates (n_{PLL}~1.8-2.7) in
121 agreement with previously reported values for peptide nanostructures.[39] FTIR
122 experiments reveal that dry PLL films exhibit primarily a β-sheet conformation (**Fig. S7**).

123 Exchange to a pH=7 buffer leads to a much larger increase in the SPR reflectivity. This
124 observation is explained by the well-known pH-mediated change in charge state of lysine
125 residues (from neutral to positively charged upon reducing the pH below ~10.6),
126 concurrent with the hydration of the PLL layer as the polypeptide chains assume a random
127 coil conformation.[40–42,20] Modeling the SPR response using a composite layer including
128 partially hydrated PLL adsorbates (10-20% hydration) shows a ~200 nm interfacial region.
129 In its hydrated state, the polypeptide layer exhibits a small but noticeable electric field-
130 dependent thickness change of ~25 nm, with the larger value at positive surface
131 potentials. The starting and end point for this thickness change depend on the assumed
132 hydration of the PLL adsorbates: 175-200 nm (10% hydration) or 210-235 nm (20%
133 hydration).

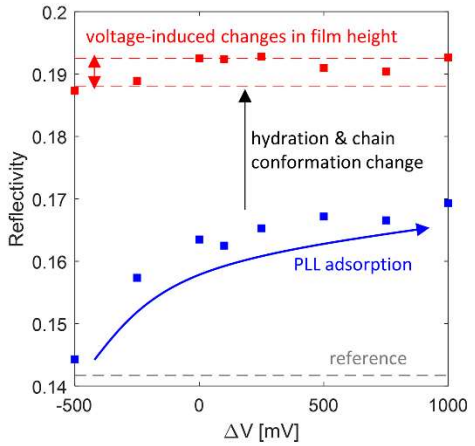

Figure 2. **Surface plasmon reflectivity can detect electric field-assisted adsorption of thin polypeptide layers from aqueous media.** Exchange from a pH=11 to a pH=7 buffer results in hydration-related changes in the charge state and conformation of PLL chains at the interface, with voltage-dependent layer thickness.

These conformational changes are further characterized using time-resolved fluorescence. The local environment at the electrode interface not only affects the conformation of polypeptide chains, it also modulates the concentration of ionic species near the electrode.

Electric field- and solvation-dependent dynamics of fluorescently labeled polypeptide chains. Beyond following time-averaged changes in film conformation, it is informative to probe the dynamic signatures of solvation and chain reorganization by measuring the time-resolved fluorescence dynamics of fluorescein (FITC) chromophores covalently attached to the polypeptide side chains. By collecting time-resolved fluorescence in two orthogonal polarizations simultaneously, it is possible to correlate fluctuations in brightness to changes in dynamic photophysical parameters such as fluorescence lifetime and/or fluorescence anisotropy (**Fig. 3**, details in Supporting Information and **Fig. S8**). We observe substantial brightness fluctuations when the PLL adsorbates are in contact

with a pH=7 buffer – up to a 45% increase in detected counts. In high pH buffer much smaller fluctuations are observed (< 20%).

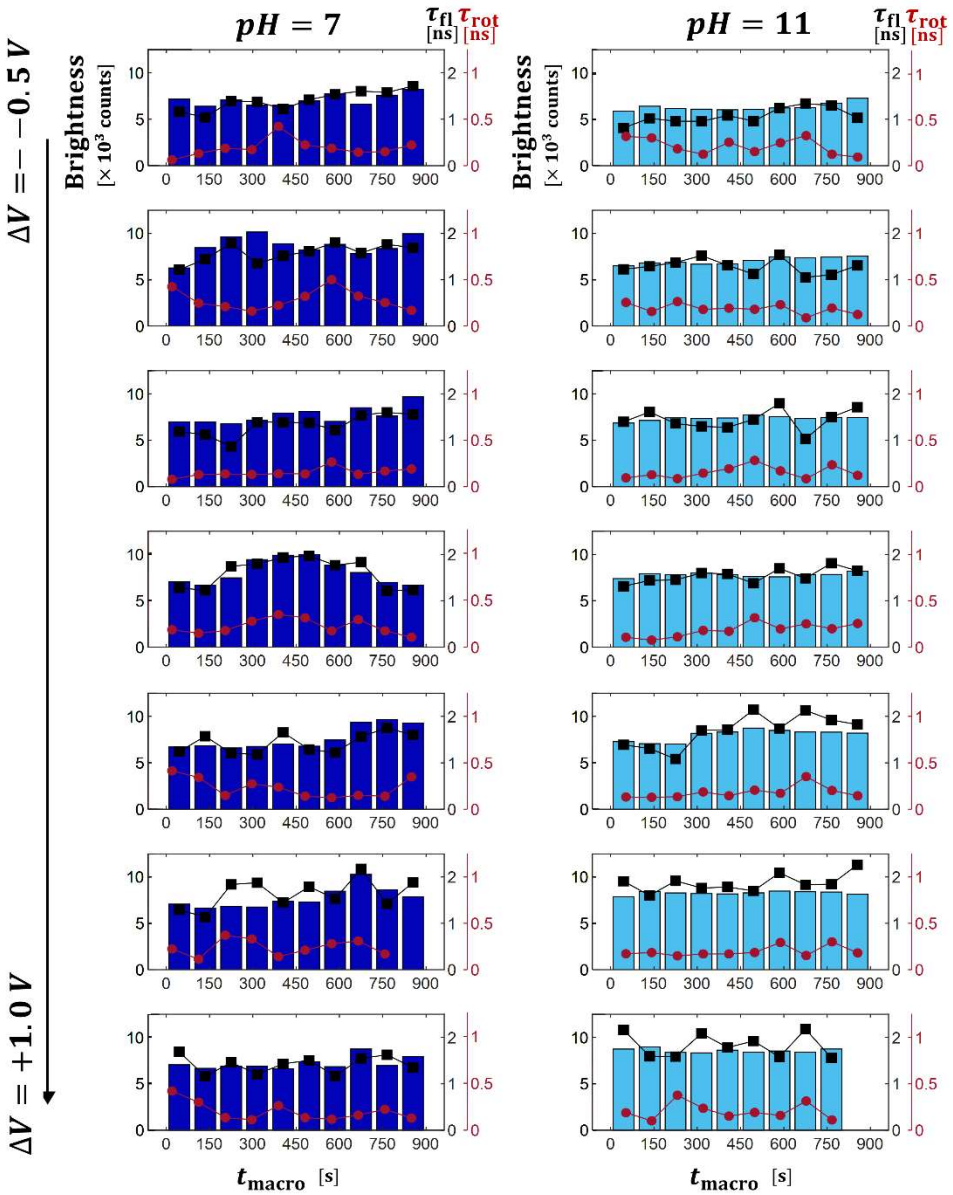

Figure 3. **Trends in time-resolved photoluminescence of adsorbed FITC-PLL on ITO as a function of voltage and pH** show that changes in hydration and chain conformation are related to brightness fluctuations. Brightness trends for FITC-PLL/ITO as a function of interfacial voltage while submerged in a pH=7 buffer (left column), or a pH=11 buffer (right column). In each panel, bars represent brightness, black squares are

the fluorescence lifetime, and red circles are rotational diffusion time. Both buffers have an ionic strength *I*=1.5 M.

149 It is informative to consider the correlation between brightness and the parameters
150 extracted from time-resolved fluorescence and anisotropy traces (**Fig. S9**). As expected
151 from the trends in **Fig. 3**, brightness fluctuations are strongly correlated with fluorescence
152 lifetime. At pH=11, FITC-labeled PLL displays relatively low fluorescence intensity with a
153 shorter and mostly constant decay lifetime of 1.5 ns. At pH=7, FITC-labeled PLL switches
154 between the dim state observed at pH=11, and a brighter state with a longer fluorescence
155 lifetime of 2 ns. A similar increase in fluorescence lifetime upon solvation of FITC dyes
156 has been also observed in core-shell porous silica nanoparticles.[43] Time-resolved
157 fluorescence anisotropy measurements allow us to monitor the rotational diffusion
158 lifetime. The rotational diffusion dynamics do not depend strongly on pH or voltage, with
159 a rotational diffusion lifetime of ~240 ps. Moderate variations in rotational diffusion lifetime
160 (fastest is ~100 ps, slowest is ~400 ps) are not correlated to the brightness. A positive
161 correlation between brightness and long-time asymptotic value of fluorescence
162 anisotropy – r(∞) – is also observed.

163 *Microenvironment within an adsorbed polypeptide layer at an electrified solid-liquid*
164 *interface.* We interpret the photophysics of FITC-PLL in relation to changes in the local
165 environment of dry or partially hydrated polypeptide adsorbates atop an electrified surface
166 in contact with high ionic strength electrolyte solutions. It is remarkable that these electric
167 field effects are observed for electrolyte solutions with large ionic strengths and
168 correspondingly short electrostatic screening lengths ($\kappa^{-1} < 1\ \mathrm{nm}$). However, it should be
169 noted that solution properties can be markedly different in the bulk vs. at the interface

170 where the partially hydrated polypeptides exist.[44,45] Additionally, effective electrostatic
171 screening at very high ionic strengths can affect the diffusive properties of charged
172 polypeptides and could be an important contributor to the dynamics observed in this
173 work.[46]

174 In aggregate, our photophysical observations are reflective of three coupled processes:
175 1) changes in the solvation state of FITC labels as a result of the overall hydration of the
176 PLL chains, 2) changes in the concentration gradient of ions, and 3) the extension of
177 charged PLL chains. These processes rely on collective motions of polypeptide chains
178 that depend on solution pH and are modulated by the interfacial electric field.

179 At pH=11, FITC labels are primarily enclosed within dehydrated PLL adsorbates and are
180 thus in a dim state, display a short fluorescence lifetime, and do not exhibit large dynamic
181 changes associated with molecular motion. However, an increase in brightness is
182 observed as the interfacial potential is increased (**Fig. S10**), likely because the interfacial
183 electric field modifies the concentration of H^+ ions within the extended boundary layer at
184 the surface of the dehydrated adsorbates.[44,45] The dependence of FITC emission on H^+
185 concentration makes it a common pH sensor, and the field-dependent brightness and
186 lifetime at pH=11 (**Fig. S11**) are consistent with FITC bulk properties. However, when
187 considering buffer pH, the overall trends measured here are opposite to what would be
188 expected in bulk solution. The lower fluorescence brightness and shorter fluorescence
189 lifetime in pH=11 (vs. pH=7) suggest that solvation state of the PLL film is the leading
190 determinant of FITC photophysics at the interface.

191 At pH=7, FITC chromophores are embedded in partially hydrated adsorbates, as
192 observed with SPR experiments. In their solvated state, PLL chains are able to

193 experience local and collective morphological transformations, which result in large
194 fluctuations in the microenvironment experienced by FITC labels attached to them. These
195 fluctuations in fluorescence brightness and lifetime are primarily due to variations in local
196 solvation. The interfacial electric field does not have a large effect on the average
197 brightness (**Fig. S10**), but a moderate reduction in the brightness fluctuations and a small
198 change in the overall thickness of the film are present at the extremes of the applied
199 surface potential range. These small electric field effects are due to the higher H^+
200 concentration and the relatively small Debye length compared to a larger portion of the
201 adsorbed layer that is hydrated and contains mobile ions.

202 The local environment near an electrode surface experienced by adsorbed polypeptide
203 chains and chromophores covalently linked to them is considerably dynamic (i.e., large
204 fluctuations) if they exist in a partially hydrated state in a high ionic strength electrolyte.
205 However, the properties of such a dynamic environment have little dependence on the
206 interfacial electric field because extended polypeptide chains are much longer than the
207 Debye screening length. When the polypeptide chains are not hydrated, they experience
208 a substantially less dynamic environment (i.e., low amplitude fluctuations) but are more
209 sensitive to changes in the interfacial properties as a result of an applied electric field. If
210 the solution atop the FITC-PLL layer is replaced with a lower ionic strength aqueous
211 electrolyte (50 mM vs. 1.5 M, **Fig. S11-12**) the amplitude of the fluctuations is low
212 irrespective of the peptide's hydration state, but a similar behavior for electric-field
213 dependence of interfacial properties is observed.

214

215

Conclusions

Electrified interfaces are a complex environment where electrode surfaces, solvent molecules, ions, and free and surface-bound species interact on multiple time scales. The microenvironment at this interface is a critical component in biomedical sensing and therapeutic devices, but also relevant for analytical separations as well as energy conversion and storage. With a combination of plasmonic and fluorescence spectroscopy probes, we gain detailed information on the molecular-scale changes in local environment and conformation at an electrified interface. The broad applicability of these tools is enabled by an instrumental platform with wide material compatibility and optimized spectral, electrical, and morphological properties.

We observe correlated changes in the reflectivity of mid-IR surface plasmon resonances and time-resolved brightness, fluorescence lifetime, and fluorescence anisotropy dynamics that probe poly-L-lysine chains at the interface of an ITO electrode. These observations reveal the interplay between solvent-dependent hydration state and collective rearrangement of adsorbed polypeptides, as well as the electric field-mediated ion concentration at the interface. A noticeable dependence of interfacial properties on applied electric field is observed at a high pH value for which dehydrated polypeptide adsorbates cover the electrode, and these properties are largely static over time. On the contrary, substantial fluctuations in the local solvation environment are observed for partially hydrated peptides at high ionic strength, but with minimal perturbations due to electric fields. A variable layer thickness is also observed upon hydration. Given that implantable bioelectronic devices are often surrounded by large ionic concentrations and at close to neutral pH (e.g., in neural tissue or blood), the presence of large fluctuations

239 in their interfacial properties can have sizable effects on device performance and stability.
240 The ability to follow coupled changes in interfacial properties enables studies where the
241 contribution of multiple processes (e.g., solvation, chain motion, quenching) can be
242 understood, exploring their co-dependence on external stimuli such as electric fields.

243

244 ***References***

245 (1) Liu, X.; Yuan, L.; Li, D.; Tang, Z.; Wang, Y.; Chen, G.; Chen, H.; Brash, J. L. Blood Compatible
246 Materials: State of the Art. *J. Mater. Chem. B* **2014**, *2* (35), 5718–5738.
247 https://doi.org/10.1039/C4TB00881B.
248 (2) Maehashi, K.; Katsura, T.; Kerman, K.; Takamura, Y.; Matsumoto, K.; Tamiya, E. Label-Free Protein
249 Biosensor Based on Aptamer-Modified Carbon Nanotube Field-Effect Transistors. *Anal. Chem.*
250 **2007**, *79* (2), 782–787. https://doi.org/10.1021/ac060830g.
251 (3) Gao, D.; Parida, K.; Lee, P. S. Emerging Soft Conductors for Bioelectronic Interfaces. *Advanced*
252 *Functional Materials n/a* (n/a), 1907184. https://doi.org/10.1002/adfm.201907184.
253 (4) Song, E.; Fang, H.; Jin, X.; Zhao, J.; Jiang, C.; Yu, K. J.; Zhong, Y.; Xu, D.; Li, J.; Fang, G.; Du, H.;
254 Zhang, J.; Park, J. M.; Huang, Y.; Alam, M. A.; Mei, Y.; Rogers, J. A. Thin, Transferred Layers of
255 Silicon Dioxide and Silicon Nitride as Water and Ion Barriers for Implantable Flexible Electronic
256 Systems. *Advanced Electronic Materials* **2017**, *3* (8), 1700077.
257 https://doi.org/10.1002/aelm.201700077.
258 (5) Eftekhari-Bafrooei, A.; Borguet, E. Effect of Electric Fields on the Ultrafast Vibrational Relaxation
259 of Water at a Charged Solid–Liquid Interface as Probed by Vibrational Sum Frequency
260 Generation. *J. Phys. Chem. Lett.* **2011**, *2* (12), 1353–1358. https://doi.org/10.1021/jz200194e.
261 (6) Lagutchev, A. S.; Patterson, J. E.; Huang, W.; Dlott, D. D. Ultrafast Dynamics of Self-Assembled
262 Monolayers under Shock Compression: Effects of Molecular and Substrate Structure. *J. Phys.*
263 *Chem. B* **2005**, *109* (11), 5033–5044. https://doi.org/10.1021/jp0450742.
264 (7) Lee, W.; Kim, D.; Matsuhisa, N.; Nagase, M.; Sekino, M.; Malliaras, G. G.; Yokota, T.; Someya, T.
265 Transparent, Conformable, Active Multielectrode Array Using Organic Electrochemical
266 Transistors. *PNAS* **2017**, *114* (40), 10554–10559. https://doi.org/10.1073/pnas.1703886114.
267 (8) Hwang, S.-W.; Tao, H.; Kim, D.-H.; Cheng, H.; Song, J.-K.; Rill, E.; Brenckle, M. A.; Panilaitis, B.;
268 Won, S. M.; Kim, Y.-S.; Song, Y. M.; Yu, K. J.; Ameen, A.; Li, R.; Su, Y.; Yang, M.; Kaplan, D. L.; Zakin,
269 M. R.; Slepian, M. J.; Huang, Y.; Omenetto, F. G.; Rogers, J. A. A Physically Transient Form of
270 Silicon Electronics. *Science* **2012**, *337* (6102), 1640–1644.
271 https://doi.org/10.1126/science.1226325.
272 (9) Bellassai, N.; Marti, A.; Spoto, G.; Huskens, J. Low-Fouling, Mixed-Charge Poly-L-Lysine Polymers
273 with Anionic Oligopeptide Side-Chains. *J. Mater. Chem. B* **2018**, *6* (46), 7662–7673.
274 https://doi.org/10.1039/C8TB01619D.
275 (10) Chen, X.; Wang, J.; Sniadecki, J. J.; Even, M. A.; Chen, Z. Probing α-Helical and β-Sheet Structures
276 of Peptides at Solid/Liquid Interfaces with SFG. *Langmuir* **2005**, *21* (7), 2662–2664.
277 https://doi.org/10.1021/la050048w.
278 (11) Rabe, M.; Verdes, D.; Seeger, S. Understanding Protein Adsorption Phenomena at Solid Surfaces.
279 *Advances in Colloid and Interface Science* **2011**, *162* (1), 87–106.
280 https://doi.org/10.1016/j.cis.2010.12.007.

(12) Kishore Sahoo, J.; S. Sirimuthu, N. M.; Canning, A.; Zelzer, M.; Graham, D.; V. Ulijn, R. Analysis of Enzyme-Responsive Peptide Surfaces by Raman Spectroscopy. *Chemical Communications* **2016**, *52* (25), 4698–4701. https://doi.org/10.1039/C5CC09189F.

(13) Kharlampieva, E.; Min Jung, C.; Kozlovskaya, V.; V. Tsukruk, V. Secondary Structure of Silaffin at Interfaces and Titania Formation. *Journal of Materials Chemistry* **2010**, *20* (25), 5242–5250. https://doi.org/10.1039/C0JM00600A.

(14) Dai, B.; Kang, S.; Huynh, T.; Lei, H.; Castelli, M.; Hu, J.; Zhang, Y.; Zhou, R. Salts Drive Controllable Multilayered Upright Assembly of Amyloid-like Peptides at Mica/Water Interface. *PNAS* **2013**, *110* (21), 8543–8548. https://doi.org/10.1073/pnas.1220711110.

(15) Shen, L.; Ulrich, N. W.; Mello, C. M.; Chen, Z. Determination of Conformation and Orientation of Immobilized Peptides and Proteins at Buried Interfaces. *Chemical Physics Letters* **2015**, *619*, 247–255. https://doi.org/10.1016/j.cplett.2014.10.035.

(16) Miller, C. E.; Majewski, J.; Gog, T.; Kuhl, T. L. Characterization of Biological Thin Films at the Solid-Liquid Interface by X-Ray Reflectivity. *Phys. Rev. Lett.* **2005**, *94* (23), 238104. https://doi.org/10.1103/PhysRevLett.94.238104.

(17) Shen, L.; Adachi, T.; Vanden Bout, D.; Zhu, X.-Y. A Mobile Precursor Determines Amyloid-β Peptide Fibril Formation at Interfaces. *J. Am. Chem. Soc.* **2012**, *134* (34), 14172–14178. https://doi.org/10.1021/ja305398f.

(18) Wei, Y.; Latour, R. A. Determination of the Adsorption Free Energy for Peptide−Surface Interactions by SPR Spectroscopy. *Langmuir* **2008**, *24* (13), 6721–6729. https://doi.org/10.1021/la8005772.

(19) Bearinger, J. P.; Vörös, J.; Hubbell, J. A.; Textor, M. Electrochemical Optical Waveguide Lightmode Spectroscopy (EC-OWLS): A Pilot Study Using Evanescent-Field Optical Sensing under Voltage Control to Monitor Polycationic Polymer Adsorption onto Indium Tin Oxide (ITO)-Coated Waveguide Chips. *Biotechnology and Bioengineering* **2003**, *82* (4), 465–473. https://doi.org/10.1002/bit.10591.

(20) Saftics, A.; Prósz, G. A.; Türk, B.; Peter, B.; Kurunczi, S.; Horvath, R. In Situ Viscoelastic Properties and Chain Conformations of Heavily Hydrated Carboxymethyl Dextran Layers: A Comparative Study Using OWLS and QCM-I Chips Coated with Waveguide Material. *Scientific Reports* **2018**, *8* (1), 1–14. https://doi.org/10.1038/s41598-018-30201-6.

(21) Allgeyer, E. S.; Sterling, S. M.; Gunewardene, M. S.; Hess, S. T.; Neivandt, D. J.; Mason, M. D. Combining Total Internal Reflection Sum Frequency Spectroscopy Spectral Imaging and Confocal Fluorescence Microscopy. *Langmuir* **2015**, *31* (3), 987–994. https://doi.org/10.1021/la5036932.

(22) Zhang, C.; Jasensky, J.; Wu, J.; Chen, Z. Combining Surface Sensitive Vibrational Spectroscopy and Fluorescence Microscopy to Study Biological Interfaces. In *Imaging, Manipulation, and Analysis of Biomolecules, Cells, and Tissues XII*; International Society for Optics and Photonics, 2014; Vol. 8947, p 894712. https://doi.org/10.1117/12.2040828.

(23) O'Callahan, B. T.; Park, K.-D.; Novikova, I. V.; Jian, T.; Chen, C.-L.; Muller, E. A.; El-Khoury, P. Z.; Raschke, M. B.; Lea, A. S. In Liquid Infrared Scattering Scanning Near-Field Optical Microscopy for Chemical and Biological Nanoimaging. *Nano Lett.* **2020**, *20* (6), 4497–4504. https://doi.org/10.1021/acs.nanolett.0c01291.

(24) Wang, Y.; Overvig, A. C.; Shrestha, S.; Zhang, R.; Wang, R.; Yu, N.; Negro, L. D. Tunability of Indium Tin Oxide Materials for Mid-Infrared Plasmonics Applications. *Opt. Mater. Express, OME* **2017**, *7* (8), 2727–2739. https://doi.org/10.1364/OME.7.002727.

(25) Rhodes, C.; Franzen, S.; Maria, J.-P.; Losego, M.; Leonard, D. N.; Laughlin, B.; Duscher, G.; Weibel, S. Surface Plasmon Resonance in Conducting Metal Oxides. *Journal of Applied Physics* **2006**, *100* (5), 054905. https://doi.org/10.1063/1.2222070.

(26) Brewer, S. H.; Franzen, S. Indium Tin Oxide Plasma Frequency Dependence on Sheet Resistance and Surface Adlayers Determined by Reflectance FTIR Spectroscopy. *J. Phys. Chem. B* **2002**, *106* (50), 12986–12992. https://doi.org/10.1021/jp026600x.

(27) Agrawal, A.; Johns, R. W.; Milliron, D. J. Control of Localized Surface Plasmon Resonances in Metal Oxide Nanocrystals. *Annual Review of Materials Research* **2017**, *47* (1), 1–31. https://doi.org/10.1146/annurev-matsci-070616-124259.

(28) Franzen, S. Surface Plasmon Polaritons and Screened Plasma Absorption in Indium Tin Oxide Compared to Silver and Gold. *J. Phys. Chem. C* **2008**, *112* (15), 6027–6032. https://doi.org/10.1021/jp7097813.

(29) Franzen, S.; Rhodes, C.; Cerruti, M.; Gerber, R. W.; Losego, M.; Maria, J.-P.; Aspnes, D. E. Plasmonic Phenomena in Indium Tin Oxide and ITO-Au Hybrid Films. *Opt. Lett., OL* **2009**, *34* (18), 2867–2869. https://doi.org/10.1364/OL.34.002867.

(30) Losego, M. D.; Efremenko, A. Y.; Rhodes, C. L.; Cerruti, M. G.; Franzen, S.; Maria, J.-P. Conductive Oxide Thin Films: Model Systems for Understanding and Controlling Surface Plasmon Resonance. *Journal of Applied Physics* **2009**, *106* (2), 024903. https://doi.org/10.1063/1.3174440.

(31) Rhodes, C.; Cerruti, M.; Efremenko, A.; Losego, M.; Aspnes, D. E.; Maria, J.-P.; Franzen, S. Dependence of Plasmon Polaritons on the Thickness of Indium Tin Oxide Thin Films. *Journal of Applied Physics* **2008**, *103* (9), 093108. https://doi.org/10.1063/1.2908862.

(32) Tandon, B.; Agrawal, A.; Heo, S.; Milliron, D. J. Competition between Depletion Effects and Coupling in the Plasmon Modulation of Doped Metal Oxide Nanocrystals. *Nano Lett.* **2019**, *19* (3), 2012–2019. https://doi.org/10.1021/acs.nanolett.9b00079.

(33) Benck, J. D.; Pinaud, B. A.; Gorlin, Y.; Jaramillo, T. F. Substrate Selection for Fundamental Studies of Electrocatalysts and Photoelectrodes: Inert Potential Windows in Acidic, Neutral, and Basic Electrolyte. *PLOS ONE* **2014**, *9* (10), e107942. https://doi.org/10.1371/journal.pone.0107942.

(34) Aydın, E. B.; Sezgintürk, M. K. Indium Tin Oxide (ITO): A Promising Material in Biosensing Technology. *TrAC Trends in Analytical Chemistry* **2017**, *97*, 309–315. https://doi.org/10.1016/j.trac.2017.09.021.

(35) Transparent electrodes for organic optoelectronic devices: a review https://www.spiedigitallibrary.org/journals/Journal-of-Photonics-for-Energy/volume-4/issue-1/040990/Transparent-electrodes-for-organic-optoelectronic-devices-a-review/10.1117/1.JPE.4.040990.full?SSO=1 (accessed Apr 20, 2020).

(36) Jonely, M.; Noriega, R. Role of Polar Protic Solvents in the Dissociation and Reactivity of Photogenerated Radical Ion Pairs. *J. Phys. Chem. B* **2020**, *124* (15), 3083–3089. https://doi.org/10.1021/acs.jpcb.9b11299.

(37) Van Tassel, P. R. Polyelectrolyte Adsorption and Layer-by-Layer Assembly: Electrochemical Control. *Current Opinion in Colloid & Interface Science* **2012**, *17* (2), 106–113. https://doi.org/10.1016/j.cocis.2011.08.008.

(38) Choi, J.-H.; Kim, S.-O.; Linardy, E.; Dreaden, E. C.; Zhdanov, V. P.; Hammond, P. T.; Cho, N.-J. Influence of PH and Surface Chemistry on Poly(l-Lysine) Adsorption onto Solid Supports Investigated by Quartz Crystal Microbalance with Dissipation Monitoring. *J. Phys. Chem. B* **2015**, *119* (33), 10554–10565. https://doi.org/10.1021/acs.jpcb.5b01553.

(39) Handelman, A.; Apter, B.; Shostak, T.; Rosenman, G. Peptide Optical Waveguides. *Journal of Peptide Science* **2017**, *23* (2), 95–103. https://doi.org/10.1002/psc.2944.

(40) Davidson, B.; Fasman, G. D. The Conformational Transitions of Uncharged Poly-L-Lysine. α Helix-Random Coil-β Structure*. *Biochemistry* **1967**, *6* (6), 1616–1629. https://doi.org/10.1021/bi00858a008.

(41) Cieślik-Boczula, K. Alpha-Helix to Beta-Sheet Transition in Long-Chain Poly-l-Lysine: Formation of Alpha-Helical Fibrils by Poly-l-Lysine. *Biochimie* **2017**, *137*, 106–114. https://doi.org/10.1016/j.biochi.2017.03.006.
(42) Wang, Y.; Chang, Y. C. Synthesis and Conformational Transition of Surface-Tethered Polypeptide: Poly(l-Lysine). *Macromolecules* **2003**, *36* (17), 6511–6518. https://doi.org/10.1021/ma034093r.
(43) Santra, S.; Liesenfeld, B.; Bertolino, C.; Dutta, D.; Cao, Z.; Tan, W.; Moudgil, B. M.; Mericle, R. A. Fluorescence Lifetime Measurements to Determine the Core–Shell Nanostructure of FITC-Doped Silica Nanoparticles: An Optical Approach to Evaluate Nanoparticle Photostability. *Journal of Luminescence* **2006**, *117* (1), 75–82. https://doi.org/10.1016/j.jlumin.2005.04.008.
(44) Klitzing, R.; Moehwald, H. Proton Concentration Profile in Ultrathin Polyelectrolyte Films. *Langmuir* **1995**, *11* (9), 3554–3559. https://doi.org/10.1021/la00009a044.
(45) Chen, A. W.; Briseno, A. L.; Santore, M. M. Tunable Fluorescence Quenching near the Graphene-Aqueous Interface. *Journal of Colloid and Interface Science* **2017**, *506*, 76–82. https://doi.org/10.1016/j.jcis.2017.07.019.
(46) Hong, L.; Granick, S. Charged Polypeptide Diffusion at a Very High Ionic Strength. *Journal of Polymer Science Part B: Polymer Physics* **2005**, *43* (23), 3497–3502. https://doi.org/10.1002/polb.20662.

Conflict of Interest

There are no conflicts of interest to declare.

Acknowledgments

The authors acknowledge use of equipment at the Utah Nanofabrication Facility and the Lassonde Entrepreneur Institute at the University of Utah. N.S. was supported from funds from the University of Utah NSF REU program (NSF REU grant 1659579).

Supporting information for "**Multimodal spectroscopic investigation of the conformation and local environment of biomolecules at an electrified interface**"

Sasha A. Moonitz, Noah Shepard, Rodrigo Noriega

University of Utah, Department of Chemistry, 315 S. 1400 E.

Salt Lake City, UT 84112

Email: noriega@chem.utah.edu; phone: (801) 579-7979

Contents

Materials and sample preparation. Details on the deposition of ITO films, preparation of buffers and sample solutions are provided below.

Deposition of ITO films. The optoelectronic properties of magnetron sputtered ITO thin films are strongly dependent on processing conditions.[1–5] Our sensors were grown on clean sapphire substrates (double-side polished, c-cut, 2.54 cm x 2.54 cm x 0.5 mm, University Wafer) via DC magnetron sputtering (Denton Discovery 18) at room temperature and with a DC power of 50 W. The vacuum chamber was evacuated to 1.9×10^{-6} Torr before it was pumped with a 99:1 argon/oxygen gas mixture to 4.34×10^{-3} Torr. Deposition was carried out for a variable time period to achieve desired film thickness. After deposition, ITO films were annealed ex-situ under nitrogen gas in a rapid thermal annealing oven (Allwin AccuThermo AW610) at a temperature of 350° C for 2 minutes. The resulting ITO films have a low surface roughness (**Fig. S1**), with a maximum root-mean-square value (R_q) of 2.15 nm – most substrates have R_q~ 1 nm.

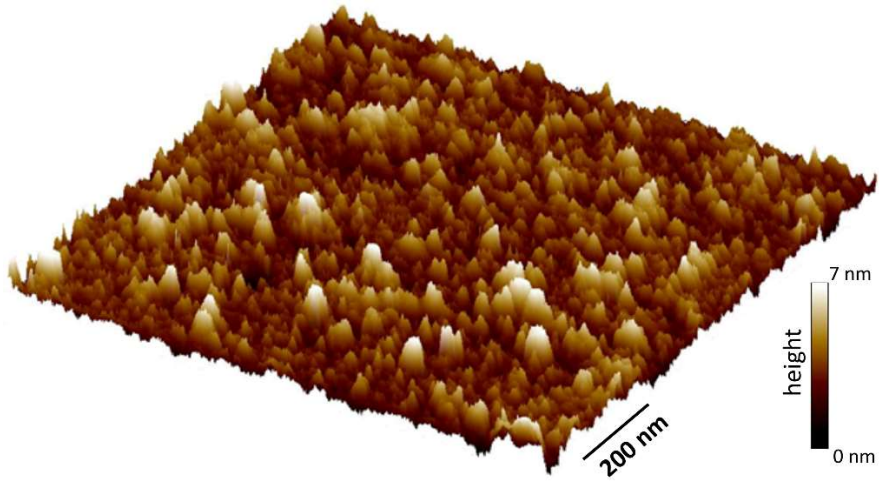

Figure S1. **Atomic force microscopy image** shows the topography of a representative section (1 μm x 1 μm) of a sputtered ITO film, with R_q = 0.93 nm.

Buffer solutions. Britton-Robinson buffer (BRB) solutions were prepared at pH=7 and pH=11 and constant ionic strengths (50 mM - 1.5 M).[6] Equimolar amounts of phosphoric acid (Sigma-Aldrich CAS 7664-38-2), glacial acetic acid (Sigma-Aldrich CAS 64-19-7),

38 and boric acid (Fisher Scientific CAS 10043-35-3) were dissolved in HPLC grade water.
39 For pH=11 buffers, 4.1 mM of each acid were used; 4.5 mM were used for pH=7 buffers.
40 The pH of each buffer was monitored with a temperature calibrated pH probe
41 (Fisherbrand Accumet AE150) and 0.1 M sodium hydroxide was added until the desired
42 pH was obtained. The ionic strengths of each solution were determined by accounting for
43 the ionic product of water, the formal concentrations of each acid and sodium hydroxide
44 at each pH, using the acid dissociation constants (**Table S1**) to determine the fractional
45 compositions of each ionic species at each pH. NaCl was used to maintain a constant
46 ionic strength between buffers.

Acid	K_1	K_2	K_3
Acetic	1.754×10^{-5}	–	–
Phosphoric	6.92×10^{-3}	6.17×10^{-8}	4.786×10^{-13}
Boric	5.37×10^{-10}	3.98×10^{-13}	5.01×10^{-14}

47 **Table S1.** Acid dissociation constants used to determine fractional compositions of ionic species
48 present in Britton-Robinson buffers of varying pH.[7]

49 *Polypeptide solutions.* Poly-L-lysine hydrochloride (PLL, Sigma-Aldrich
50 CAS # 26124-78-7, m.w. > 30 kDa) was dissolved in pH 11 BRB solutions at a
51 concentration of 1 mg/mL and used for adsorption to the ITO surface. For samples used
52 in fluorescence experiments, an identical procedure was employed but with fluorescein
53 isothiocyanate labelled poly-L-lysine (FITC-PLL, Sigma-Aldrich SKU P3069, m.w. 30 –
54 70 kDa).

55 **Optical characterization of ITO films.** Spectroscopic ellipsometry measurements were
56 conducted immediately after film deposition. This allowed validation of successful thin film
57 deposition prior to incorporation into electrochemical, fluorescence, or plasmonic
58 experiments. To avoid artifacts in the data, the back side of the substrate was sanded

into a diffusive surface. Due to the destructive nature of this characterization step, a sacrificial glass substrate was added to all film deposition runs. Data was collected with a J.A. Woollam variable-angle spectroscopic ellipsometry (VASE) instrument; analysis was performed with the instrument's onboard analysis software. Standard materials parameters were used for Cauchy models of the glass substrate and air interface. A Drude model was employed for the ITO film.[8–10] The ITO film thickness was allowed to vary in the fitting routine, and thickness values were in agreement with profilometry measurements. Materials parameters obtained for ITO films were a plasma frequency $\omega_p = 2.2 - 3.1 \times 10^{15}\ \mathrm{Hz}$ and damping coefficient $\Gamma = 2.5 \times 10^{14}\ \mathrm{Hz}$. These plasma frequencies correspond to a free carrier density $n_e = 0.5 - 1.1 \times 10^{21}\ \mathrm{cm}^{-3}$. A typical spectroscopic ellipsometry data set is shown in **Fig. S2**.

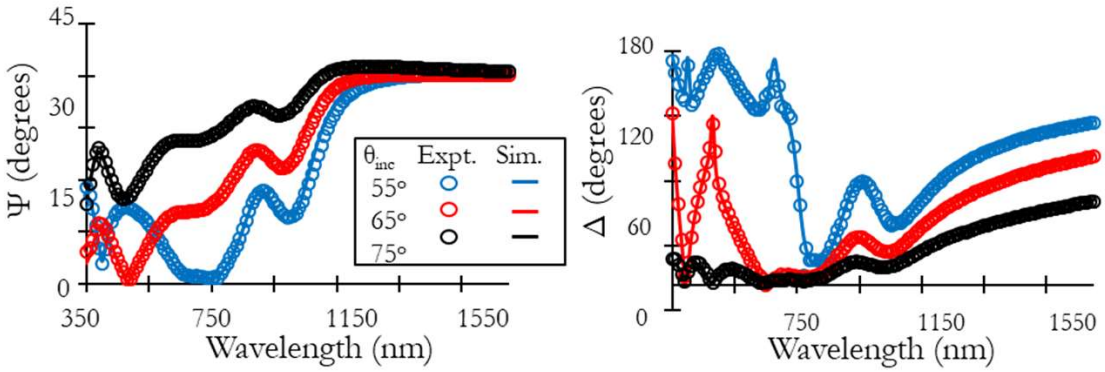

Figure S2. **Spectroscopic ellipsometry measurements on glass/ITO/air film stacks** can determine the optical constants of sputtered ITO films, which are then fit to a Drude model.

<u>SPR experimental setup.</u> Reflectivity as a function of incidence angle was measured using CW and pulsed light sources (4.5 mW of λ_{CW}=1550 nm Thorlabs LDM1550; or 100-200 μW of λ_{fs}=2500 nm from a TOPAS Prime OPA pumped by a Coherent Astrella, 5 kHz repetition rate, 40 fs pulse duration). Incident light was directed to the SPR chips using SF11 right-angle coupling prisms glued to the back side of the sapphire substrate with UV-cured high refractive index epoxy (Norland NOA170). Fully assembled SPR chips

were mounted onto a homebuilt flow cell made with chemically resistant material (Kel-F) and placed on a rotation stage; detection optics are mounted on a concentric rotation stage for θ-2θ scans. The *p*-polarized incident light was focused onto the SPR chip through the coupling prism with a Au spherical mirror with *f*=125 mm focal length. The reflected beam was measured with a biased InGaAs photodiode (Thorlabs DET10D2) whose output was fed to a lock-in amplifier (Ametek Signal Recovery) interfaced via a data acquisition card (National Instruments). A beam chopper is included in the SPR line to enable lock-in detection, and a sapphire beam sampler is used to split off a small portion of the incident beam, which is directed to an identical detection setup as the reflected beam and serves as a reference to eliminate fluctuations in laser power.

Modeling of SPR response and sensitivity estimation. Modeling of surface plasmon resonances was performed using the Winspall software package by Res-Tec, which employs the Fresnel formalism to calculate reflectivity curves of a planar film stack with dielectric properties and thicknesses that are either user-defined or least-squares fitted to data. When performing a fitting routine, only parameters corresponding to the ITO layer were allowed to vary; material properties for sapphire, SF11 glass, air, water, and methanol were fixed at reported literature values.[11–15] A small (<2 deg.) systematic deviation in experimental vs. predicted angles is due to an offset in the rotation axis and geometric center of the prism-substrate assembly, as well as minor angular deviations during prism mounting. After fitting the thickness and dielectric properties of the ITO film using their SPR response over a wide range of angles and in contact with multiple dielectric media, these parameters were fixed for constant-angle SPR reflectivity measurements.

Using the change in the SPR response for the same ITO film and different dielectric media, it is possible to estimate the sensitivity of our experiments to changes in the refractive index of the sample. Since probing condensed phases is the primary interest, the SPR reflectivity at the ITO/H_2O and ITO/MeOH are compared. The difference in the measured reflectivity $\Delta R = R_{\mathrm{MeOH}} - R_{\mathrm{H_2O}}$ is divided by the difference in the sample refractive index $\Delta n = n_{\mathrm{MeOH}} - n_{\mathrm{H_2O}}$ to approximate the sensitivity ${\mathrm{d}R}/{\mathrm{d}n} \approx {\Delta R}/{\Delta n}$. As expected given the good agreement of individual reflectivity curves with Fresnel models, observations and predictions for sensitivity match quite well (**Fig. S3**). The maximum measured sensitivity is ${\Delta R}/{\Delta n} = 4.75$. Our setup can routinely measure reflectivity values with a resolution better than 10^{-3}, which would correspond to resolvable changes in refractive index of 2×10^{-4} or better.

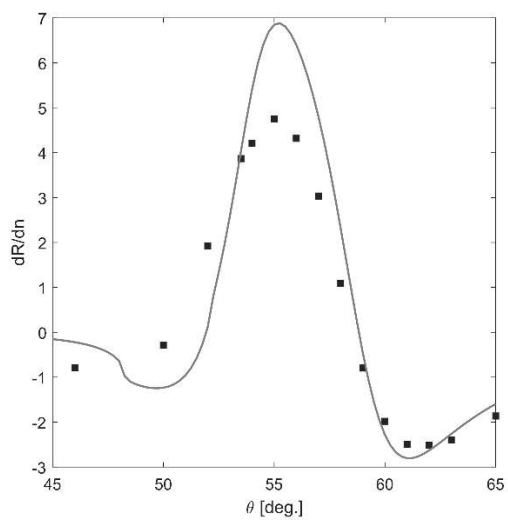

Figure S3. **Estimation of the SPR sensitivity** by considering the difference in reflectance for two simple dielectric media (water and methanol) measured sequentially in the same ITO SPR chip. The difference in reflectivity divided by the difference in refractive index is shown (experimental data as markers, model as continuous line).

<u>Electrochemical flow cell setup.</u> ITO chips were mounted in a custom three-electrode electrochemical flow cell (**Fig. S4**) driven by a bipotentiostat (CH Instruments CHI700E).

The ITO sensors could be either mounted freely (TRPL) or bonded to a high refractive index prism (SPR). Copper tape was adhered to the surface of the ITO thin film, enabling its wiring as the working electrode. A 2 mm diameter platinum wire served as the counter electrode. A 2 mm diameter Ag wire was soaked in a sodium hypochlorite solution and used as a quasi-reference electrode (QRE). The open circuit potential of the Ag QRE was measured against a Ag/AgCl reference electrode (CH Instruments CHI111) and found to maintain a potential of -67 mV in saturated KCl solutions. During potential-driven adsorption experiments, voltage was applied to the ITO working electrode for 15 minutes, after which the SPR signal was recorded and compared to the reference signal when no potential was applied. The sample solution was then flowed and the adsorption and data collection procedure were repeated for all potentials studied. Time-resolved photoluminescence studies examined the fluorescent signal of FITC-PLL already adsorbed on an ITO substrate.

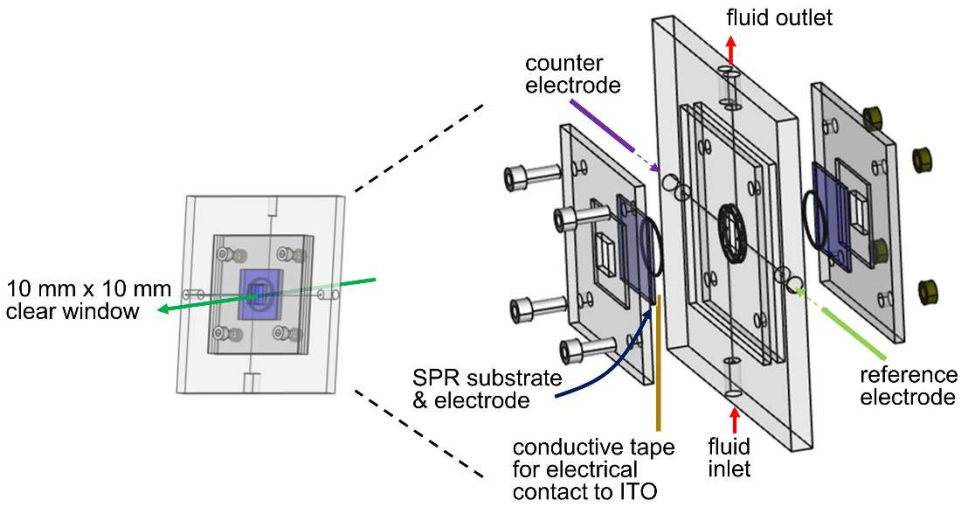

Figure S4. **Assembly of our electrochemical flow cell** designed to couple electrochemical and spectroscopic characterization of interfacial processes. Wiring connecting the working (ITO), counter (Pt), and reference (Ag/AgCl) electrodes to the bipotentiostat is not shown.

125 **Time- and polarization-resolved fluorescence of polypeptide adsorbates.** Excitation
126 pulses were 150 μW of 490 nm excitation from the second harmonic of a tunable
127 Ti:sapphire laser (Coherent Chameleon Ultra II, 80 MHz, <200 fs pulse duration) directed
128 to the sample with a 530 nm long-pass dichroic, then focused with a single 75 mm focal
129 length aspheric lens. Fluorescence was collected with the same lens, filtered with the
130 long-pass dichroic and an additional long-pass filter (580 nm cutoff). Fluorescence was
131 split into two orthogonal polarization channels and directed with large core optical fibers
132 to identical single-photon Si photodiodes (MPD Systems) whose signal was routed to a
133 TCSPC module (PHR 800 and Picoharp 300, PicoQuant). Data was acquired in a time-
134 tagged time-resolved (T3) mode that incorporates full tagging of photon detection events
135 with micro time (excitation-emission delay, 0-12.5 ns) and macro time (experimental
136 frame for synchronization to stimuli). Identical ITO substrates were loaded onto a
137 homebuilt flow cell; no SPR coupling prism was attached for these fluorescence
138 experiments. A solution of FITC-PLL (1 mg/mL in pH 11.48 BRB, *I*=1.5 M) was flowed
139 into the sample cell and the interfacial potential was stepped between -0.5–1.0 V to
140 undergo the same adsorption monitored with SPR experiments. The sample cell was
141 flushed with HPLC water several times to ensure that the only FITC-PLL remaining in the
142 flow cell was that which had adsorbed to the ITO surface, as determined when no change
143 in detected fluorescence was observed after 2 consecutive rinses (**Fig. S5**). Fluorescence
144 data was collected for 15 minutes at each of the experimental conditions (pH, voltage) for
145 which the first 2 minutes were in open circuit, then 12 minutes of applied potential,
146 followed by 1 minute at open circuit. Buffer solution was flushed through for 5 minutes in
147 between each set of experiments.

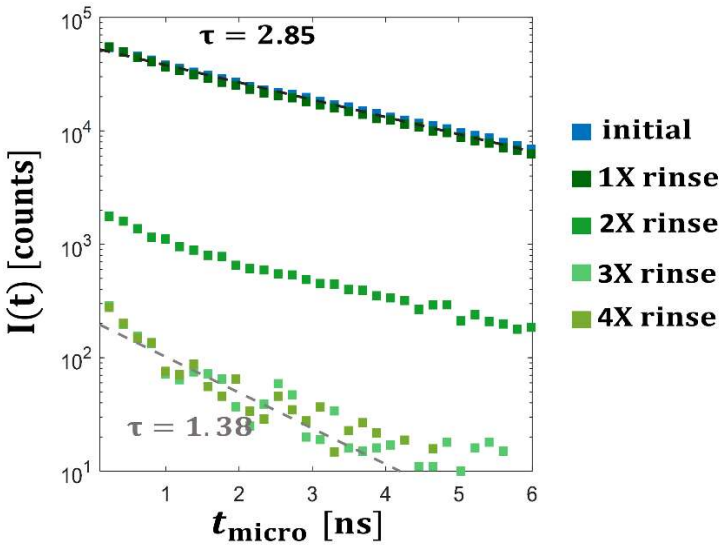

Figure S5. **Fluorescence decay traces of FITC-PLL during adsorption and subsequent rinses** show a decrease to a steady state corresponding to signal from the adsorbed film and not residual sample in solution. A substantial decrease in fluorescence lifetime is also observed for bulk vs. adsorbed species.

Morphology of adsorbed polypeptide layer. Following the electric-field assisted deposition of PLL onto the ITO surface, atomic force microscopy reveals a partial coverage of the ITO with PLL islands of variable height (**Fig. S6**). The volume fraction of PLL, Φ_{PLL}, can be calculated using AFM height maps as the volume between the topographical surface and the mean ITO baseline. For two nominally identical samples, a layer height of 75-80 nm above the mean ITO level was obtained. In each of these samples, the average PLL volume fraction over the entire AFM scans was Φ_{PLL}~3%. However, considering the variability of coverage (**Fig. S6**), it is illustrative to calculate the PLL volume fraction in the adhered layer within smaller regions (2x2 μm). With these local averages, a noticeable population of regions with a PLL volume fraction Φ_{PLL}~8.5% can be observed.

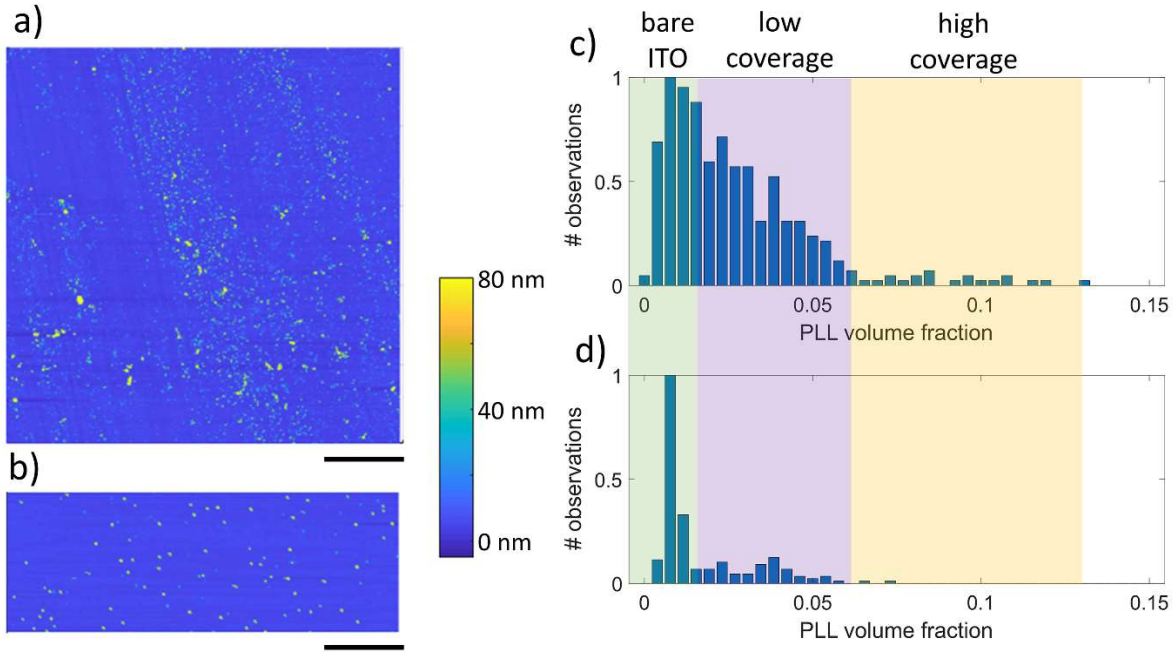

Figure S6. **Atomic force microscopy image of PLL adsorbates** atop ITO after electric-field assisted deposition from solution. Scale bar = 10 μm. Pseudo-color representations of the sample topography (on the same color scale) are shown on panels (a,b) on the left. A histogram of local PLL volume fractions (in 2x2 μm squares) for the two samples (a→ c, b→d). Shaded areas denote those regions with high ($\langle\Phi_{\mathrm{PLL}}\rangle\sim 8.5\%$) and low ($\langle\Phi_{\mathrm{PLL}}\rangle\sim 4\%$) PLL coverage, as well as those where mostly bare ITO is observed ($\langle\Phi_{\mathrm{PLL}}\rangle < 1\%$).

<u>Assessing the hydration state of PLL adsorbates.</u> To model the SPR reflectivity upon sample adsorption, an interfacial layer was inserted in the model atop the ITO surface with a thickness (75-80 nm) and coverage (3-8.5%) that are representative of those measured for PLL adsorbates (**Fig. S6**). With this geometry, the layer's thickness and dielectric properties were optimized to match the observed change in reflectivity (h=80 nm, $n_{boundary}$=1.304). If the refractive index of the mixed layer is approximated as the weighted average of its components, the refractive index of the PLL adsorbates can be estimated in the range n_{PLL}=1.8-2.7 (depending on the PLL volume fraction). This range for n_{PLL} is in agreement with values reported for poly-alanine nanostructures (n_{FFF}=1.53 @ 840 nm)[16], considering that the molar residue refractivity of lysine is twice

169 as large as that of alanine[17] and refractive indices decrease slowly at longer wavelengths
170 in the absence of resonances.

171 The small changes in reflectivity observed upon perturbation of the interface are easily
172 detected when the rotation stage and all detection optics are kept fixed. However, these
173 changes would be smaller than those resulting from positioning errors in the rotation
174 stage, which prevents the acquisition of full SPR curves as a function of continually
175 changing interfacial conditions. Thus, fixed-angle measurements provide useful
176 information regarding the interfacial layer but rely on assumptions on its properties – e.g.,
177 minimal changes in hydration while at constant pH. In this way, we account for the
178 average thickness of the adsorbed PLL layer assuming various hydration levels. For the
179 minimum (0.188) and maximum (0.193) values of reflectivity observed, average thickness
180 of the PLL adsorbed layer would be in the 175-200 nm range (adsorbates with 10%
181 hydration) or 210-235 nm range (adsorbates with 20% hydration).

182 **Fourier-transform infrared spectroscopy of PLL samples.** While the transparency
183 window of sapphire extends to ~ 6 μm, large path lengths through aqueous solutions
184 prevent the use of standard FTIR transmission measurements. To verify that our
185 polypeptide samples display the expected conformations in dry and solvated
186 environments, we performed FTIR absorbance experiments in transmission geometry for
187 dry PLL films atop blank sapphire substrates, and for concentrated PLL solutions in
188 methanol sandwiched between sapphire windows using a 6 μm spacer (**Fig. S7**). While
189 these conditions are different from those used in SPR and TRPL experiments, they
190 suggest that the poly-L-lysine samples used (~200 residues long chains) experience

similar conformational changes as those previously reported in the literature. Data were collected with a Thermo Scientific Nicolet iS50 spectrometer (transmission configuration).

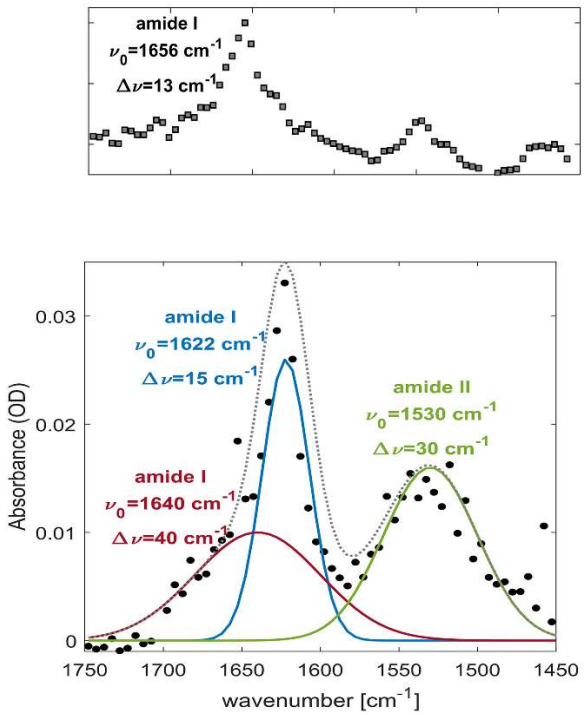

Figure S7. **FTIR spectra of dry PLL on sapphire** show peaks in the amide I and II regions. The amide I band can be used to assess secondary structure. In a dry film (bottom panel), peaks at 1622 cm^{-1} and 1640 cm^{-1} are characteristic of β-sheets. Top panel shows data for concentrated PLL solution in methanol with 63 mM of HCl, whose peak at 1656 cm^{-1} is characteristic of α-helices.[16]

<u>Time-resolved fluorescence lifetime and anisotropy of polypeptide adsorbates at an electrified solid/liquid interface.</u> The raw data for the TRPL experiments performed in this work are photon detection events, tagged by channel (V or H polarization) and their detection time (micro time and macro time). Binning these data by channel and macro time allows for brightness trends. Histograms of micro time for a particular channel contain fluorescence lifetime decay data. Differences in arrival time for each channel due to different optical and/or electronic path lengths are accounted for with a horizontal shift.

Differences in collection efficiency for V/H polarization channels make it is necessary to equalize the counts in these channels before calculating rotationally averaged

fluorescence decays traces and time-resolved fluorescence anisotropy. This is done by the tail-matching method, where a specific sample is approximated as freely-diffusing chromophore and its long-time values of V/H-polarized fluorescence are matched with a scaling factor *g* for one of them so that the ensuing anisotropy decays to zero. Because the V/H channel equalization factor *g* is an instrument variable, it is kept fixed for all other samples. In our setup, *g*=0.205. The resulting rotationally averaged fluorescence decay and time-resolved fluorescence anisotropy are given by **Eq. S1** and **S2**, respectively.

$$I_{tot}(t) = I_V(t) + 2g \cdot I_H(t) \quad \textbf{Eq. S1}$$

$$r(t) = \frac{I_V(t) - g \cdot I_H(t)}{I_V(t) + 2g \cdot I_H(t)} \quad \textbf{Eq. S2}$$

The tail-matched data are binned as a function of macro time into 90 s periods, and the micro time histograms for photons detected within that observation window are used to compute fluorescence lifetime and time-resolved anisotropy traces, which are fitted as single exponential decays with a nonlinear least-squares routine. Typical traces are shown in **Fig. S8**. Due to the small amount of sample, the resulting count rates are low (~35-150 cps) which prevented accurate determination of fitted parameters in a small subset of data points (observations at t_{macro}>800 s in pH=7 at ΔV_{ITO}=750 mV and in pH=11 at ΔV_{ITO}=1 V, both for *I*=1.5 M).

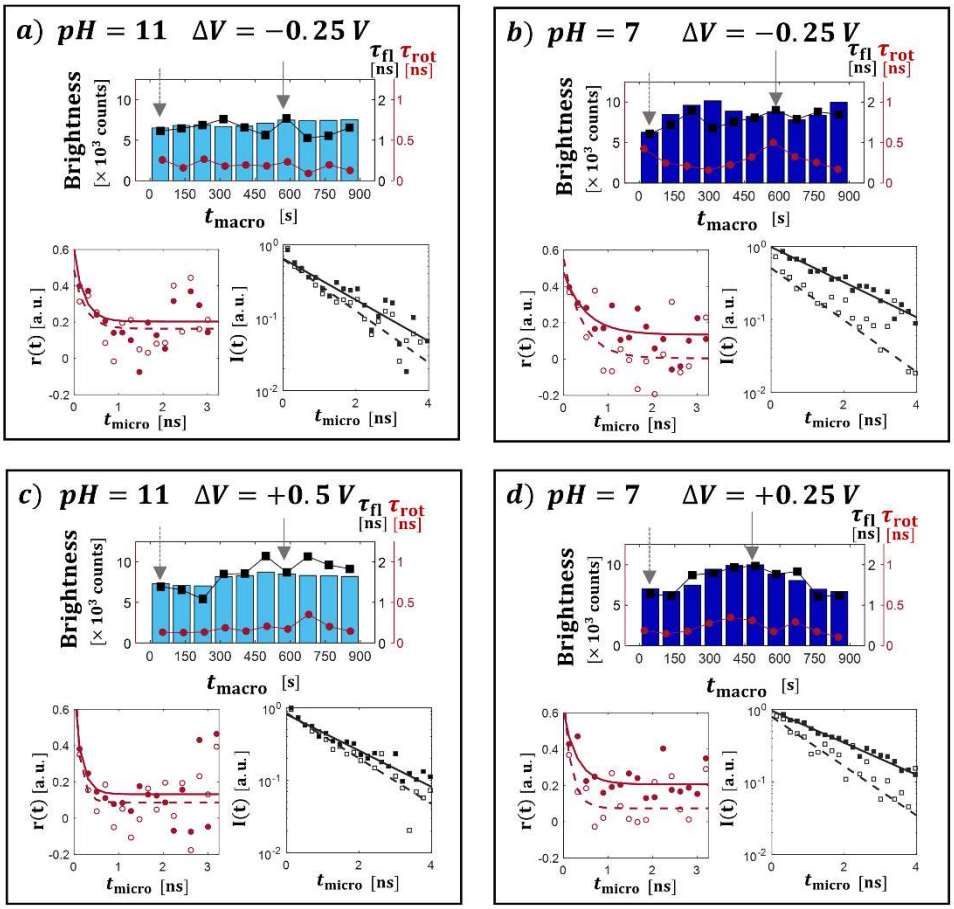

Figure S8. **Representative examples of time-resolved fluorescence I(t) and time-resolved fluorescence anisotropy r(t)** of FITC-PLL adsorbed on ITO substrates, as a function of the buffer pH and interfacial voltage. For each pH and ΔV set (a,b,c,d), two time points are chosen – one depicting the early dynamics before voltage is applied and another time point after the interfacial potential has been applied (denoted by gray arrows). The no-voltage dynamics are shown by empty markers (data) and dashed lines (fit); solid markers and solid lines depict the data and fit for the dynamics under applied voltage, respectively.

The correlation between brightness and photophysical parameters is supported by the trends shown in **Fig. S9**. The sample brightness shows a clear positive correlation with fluorescence lifetime τ_{fl} and with the asymptotic fluorescence anisotropy value $r(\infty)$. Brightness does not show a noticeable correlation with either rotational diffusion time scale τ_{rot} nor with the initial fluorescence anisotropy value $r(0)$.

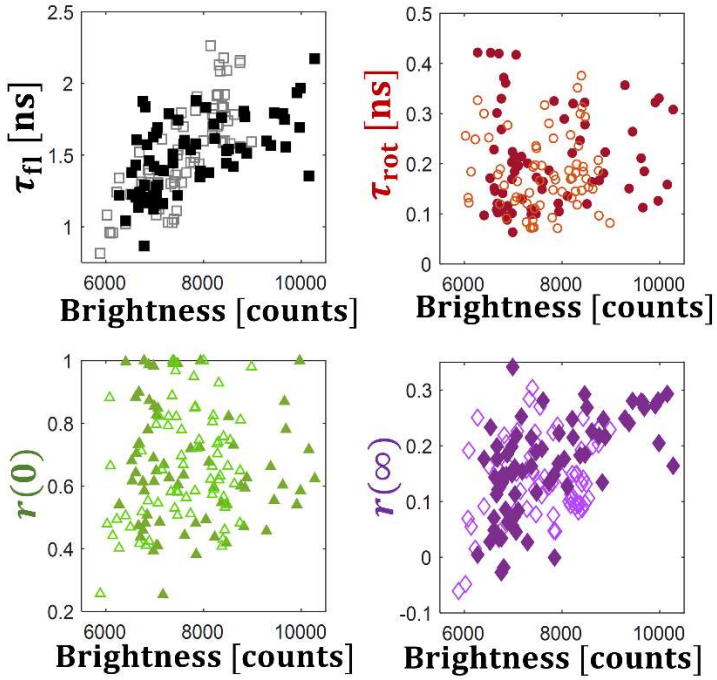

Figure S9. **Fluorescence brightness** shows a noticeable positive correlation with fluorescence lifetime and asymptotic anisotropy value, and no correlation with rotational diffusion time or initial anisotropy value. Filled markers correspond to data in pH=7 buffer, empty markers are pH=11 data.

The dependence of mean brightness and the presence of fluctuations as a function of voltage display a discernible voltage trend at pH=11, and weak correlation with voltage at pH=7 (**Fig. S10**).

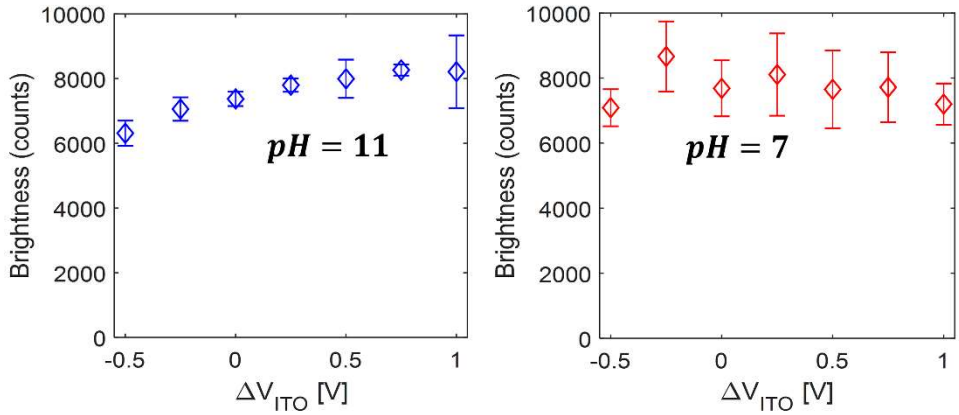

Figure S10. **Voltage dependent mean brightness and its standard deviation** show a slight increase in brightness with more positive voltages at pH=11, with negligible fluctuations. At pH=7, the fluctuations are much more significant, and no trend is observed for their brightness.

<u>Effect of ionic strength on interfacial dynamics.</u> To investigate the role of ionic strength in the observed trends, the time-resolved fluorescence experiments described above were repeated after replacing the solution in the flow cell with buffered electrolytes with an ionic strength of 50 mM, for both pH values (pH=11 and pH =7, **Fig. S11**).

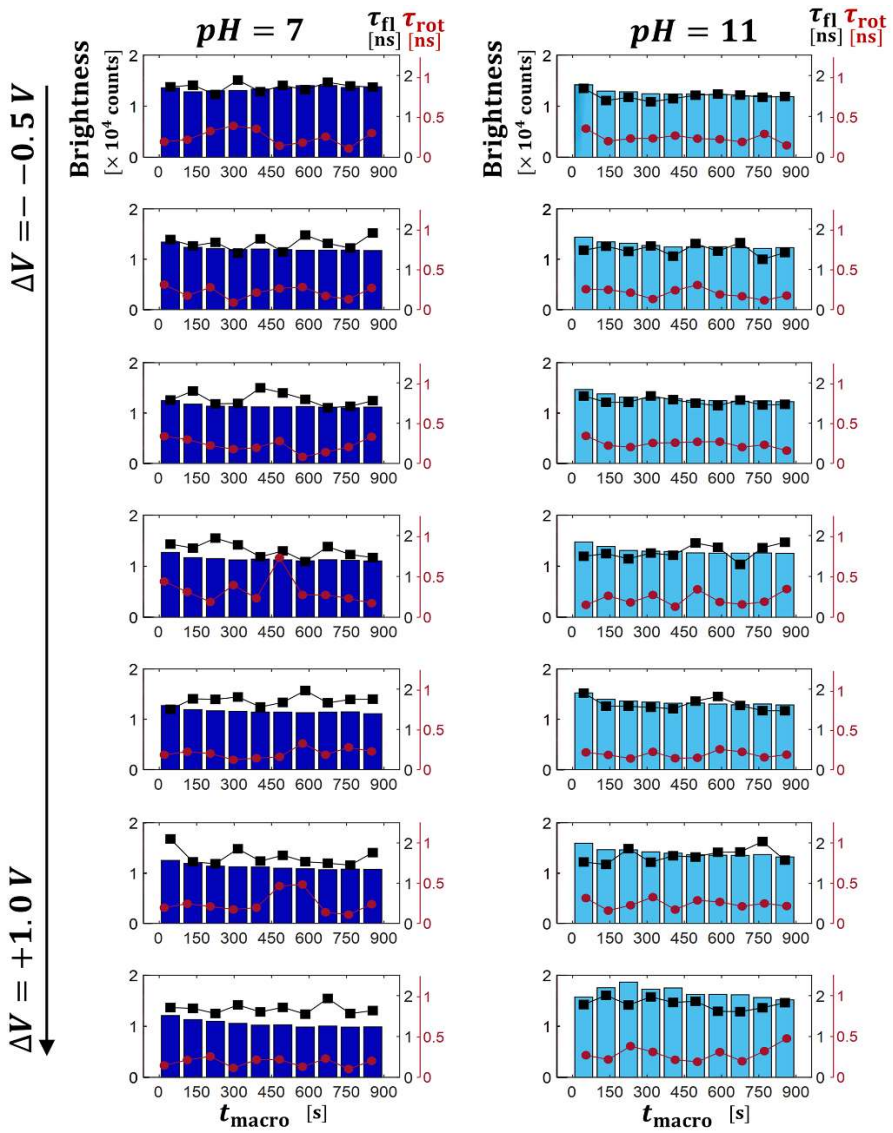

Figure S11. **Low ionic strength behavior of the time-resolved photoluminescence of adsorbed FITC-PLL on ITO as a function of voltage and pH,** equivalent to data for high ionic strength solutions in **Fig. 3**. Brightness trends for FITC-PLL adsorbed on ITO as a function of interfacial voltage while submerged in a pH=7 buffer (left), or a pH=11 buffer (right). Bars represent brightness, black squares are the fluorescence lifetime, and red circles are rotational diffusion time.

At this lower ionic strength, FITC-PLL adsorbates in contact with low- or high-pH solutions display a low amplitude of fluctuations (< 20%). Similar to the data in high ionic strength solutions, the applied electric field affects the photophysics of high pH samples, with little effects on the properties of samples at low pH (**Fig. S12**).

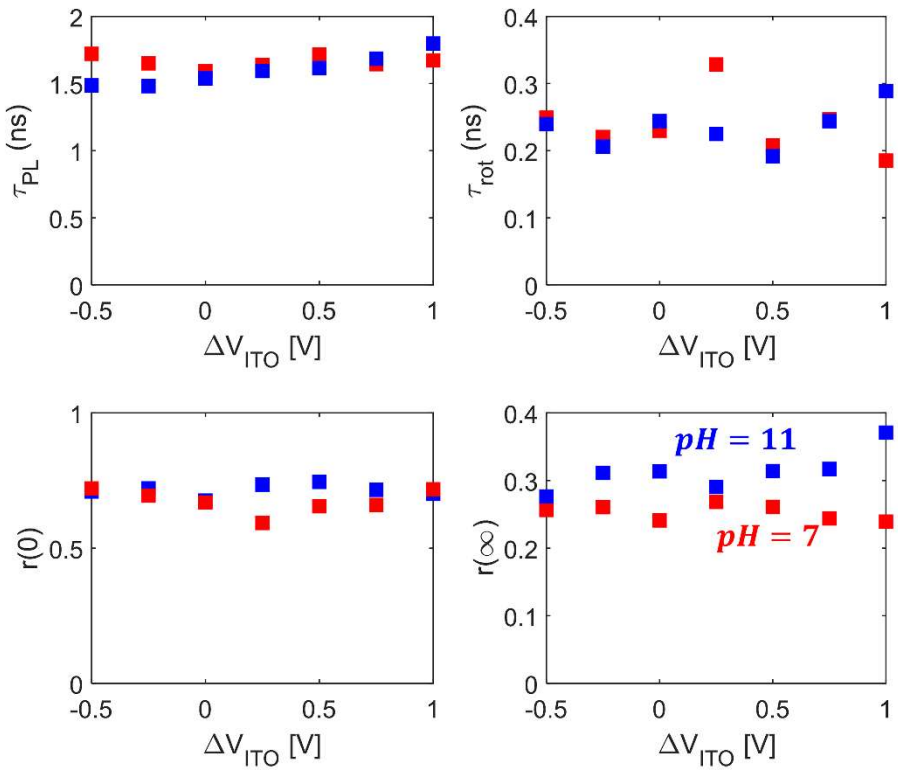

Figure S12. **At lower ionic strength, the voltage dependent photophysics of FITC-PLL** display a slight increase in fluorescence lifetime τ_{PL} and asymptotic anisotropy value $r(\infty)$ as voltage increases at pH=11. All other parameters show no voltage dependence. Plots show the average values for each voltage; blue markers are data at pH=11, red markers are data at pH=7. Buffer ionic strength for these experiments was 50 mM.

<u>Safety and Hazards statement.</u> Hazards associated with this work are primarily due to the use of non-ionizing radiation (Class IV laser systems), as well as high power electrical equipment (DC magnetron sputtering).

References.

(1) Park, J. H.; Buurma, C.; Sivananthan, S.; Kodama, R.; Gao, W.; Gessert, T. A. The Effect of Post-Annealing on Indium Tin Oxide Thin Films by Magnetron Sputtering Method. *Applied Surface Science* **2014**, *307*, 388–392. https://doi.org/10.1016/j.apsusc.2014.04.042.

(2) Wu, W.-F.; Chiou, B.-S.; Hsieh, S.-T. Effect of Sputtering Power on the Structural and Optical Properties of RF Magnetron Sputtered ITO Films. *Semicond. Sci. Technol.* **1994**, *9* (6), 1242–1249. https://doi.org/10.1088/0268-1242/9/6/014.

(3) Kim, H.; Horwitz, J. S.; Kushto, G.; Piqué, A.; Kafafi, Z. H.; Gilmore, C. M.; Chrisey, D. B. Effect of Film Thickness on the Properties of Indium Tin Oxide Thin Films. *Journal of Applied Physics* **2000**, *88* (10), 6021–6025. https://doi.org/10.1063/1.1318368.

(4) Ray, S.; Banerjee, R.; Basu, N.; Batabyal, A. K.; Barua, A. K. Properties of Tin Doped Indium Oxide Thin Films Prepared by Magnetron Sputtering. *Journal of Applied Physics* **1983**, *54* (6), 3497–3501. https://doi.org/10.1063/1.332415.

(5) Bender, M.; Seelig, W.; Daube, C.; Frankenberger, H.; Ocker, B.; Stollenwerk, J. Dependence of Oxygen Flow on Optical and Electrical Properties of DC-Magnetron Sputtered ITO Films. *Thin Solid Films* **1998**, *326* (1), 72–77. https://doi.org/10.1016/S0040-6090(98)00521-5.

(6) Mongay, C.; Cerda, V. A Britton-Robinson Buffer of Known Ionic Strength. *Analli di Chim.* **1974**, *64*, 409–412.

(7) *CRC Handbook of Chemistry and Physics*, 97th ed.; Haynes, W. M., Lide, D. R., Bruno, T. J., Eds.; CRC Press: Boca Raton.

(8) Synowicki, R. A. Spectroscopic Ellipsometry Characterization of Indium Tin Oxide Film Microstructure and Optical Constants. *Thin Solid Films* **1998**, *313–314*, 394–397. https://doi.org/10.1016/S0040-6090(97)00853-5.

(9) Brewer, S. H.; Franzen, S. Optical Properties of Indium Tin Oxide and Fluorine-Doped Tin Oxide Surfaces: Correlation of Reflectivity, Skin Depth, and Plasmon Frequency with Conductivity. *Journal of Alloys and Compounds* **2002**, *338* (1), 73–79. https://doi.org/10.1016/S0925-8388(02)00217-7.

(10) Brewer, S. H.; Franzen, S. Indium Tin Oxide Plasma Frequency Dependence on Sheet Resistance and Surface Adlayers Determined by Reflectance FTIR Spectroscopy. *J. Phys. Chem. B* **2002**, *106* (50), 12986–12992. https://doi.org/10.1021/jp026600x.

(11) Moutzouris, K.; Papamichael, M.; Betsis, S. C.; Stavrakas, I.; Hloupis, G.; Triantis, D. Refractive, Dispersive and Thermo-Optic Properties of Twelve Organic Solvents in the Visible and near-Infrared. *Appl. Phys. B* **2014**, *116* (3), 617–622. https://doi.org/10.1007/s00340-013-5744-3.

(12) Hale, G. M.; Querry, M. R. Optical Constants of Water in the 200-Nm to 200-Mm Wavelength Region. *Appl. Opt., AO* **1973**, *12* (3), 555–563. https://doi.org/10.1364/AO.12.000555.

(13) Weber, M. J. *Handbook of Optical Materials*; 2003.

(14) Optical Glass Data Sheets. SCHOTT.

(15) Mathar, R. J. Refractive Index of Humid Air in the Infrared: Model Fits. *J. Opt. A: Pure Appl. Opt.* **2007**, *9* (5), 470–476. https://doi.org/10.1088/1464-4258/9/5/008.

(16) Handelman, A.; Apter, B.; Shostak, T.; Rosenman, G. Peptide Optical Waveguides. *Journal of Peptide Science* **2017**, *23* (2), 95–103. https://doi.org/10.1002/psc.2944.

(17) Zhao, H.; Brown, P. H.; Schuck, P. On the Distribution of Protein Refractive Index Increments. *Biophys J* **2011**, *100* (9), 2309–2317. https://doi.org/10.1016/j.bpj.2011.03.004.
(18) Mirtič, A.; Grdadolnik, J. The Structure of Poly-l-Lysine in Different Solvents. *Biophysical Chemistry* **2013**, *175–176*, 47–53. https://doi.org/10.1016/j.bpc.2013.02.004.